Mecánica Computacional Vol. XXIII, pp. 209-228
G.Buscaglia, E.Dari, O.Zamonsky (Eds.)
Bariloche, Argentina, November 2004

MODELING OF CRACK PROPAGATION IN THIN-WALLED STRUCTURES

Pablo D. Zavattieri

GM Research and Development Center
30500 Mound Rd.
Warren, MI, U.S.A.
e-mail: pablo.zavattieri@gm.com

Key Words: Crack propagation, fracture, cohesive zone model, thin-walled structures, shell elements.

Abstract. *A cohesive interface element is presented for the finite element analysis of crack growth in thin specimens. In this work, the traditional cohesive interface model is extended to handle cracks in the context of three-dimensional shell elements. In addition to the traction-displacement law, a bending moment-rotation relation is included to transmit the moment and describe the initiation and propagation of cracks growing through the thickness of the shell elements. Since crack initiation and evolution are a natural outcome of the cohesive zone model without the need of any ad-hoc fracture criterion, this model results in automatic prediction of fracture. In particular, this paper will focus on cases involving Mode I/III fracture and bending, typical of complex cases existing in industrial applications in which thin-walled structures are subjected to extreme loading conditions (e.g., crashworthiness analysis). Finally, we will discuss how the three-dimensional effects near the crack front may affect the determination of the cohesive parameters to be used with this model.*

1 INTRODUCTION

The Cohesive Zone Model (CZM) has gained significant importance in the modeling of crack propagation in solids in recent years. Although this model was first proposed by Barenblatt in 1962[1] to describe material degradation and separation in a process zone in front of the crack tip in brittle materials and then applied to ductile fracture by Dugdale in 1959[2]; most of the advances in the implementation of this model into numerical methods have taken place during the last decade[3,4,5,6,7].

The most commonly used technique to incorporate the cohesive zone model into a finite element analysis is the discrete representation of the crack which is accomplished by introducing cohesive surfaces (or so-called zero-thickness interface elements) along inter-element boundaries. In most cases, these special elements are governed by a cohesive constitutive law that relates the traction with the opening and shear displacement across the interface[3-7]. Although, other techniques that make use of smeared or exact representation of the crack regardless the initial mesh have been developed in last few years[8,9,10], the utilization of interface elements remains attractive essentially due to the simplicity and effectiveness in some applications. In fact, the main advantage is that the complexity of crack initiation and evolution (including branching, coalescence and arrest) can be modeled as a natural outcome of the model, without the need of any additional fracture criterion.

The first efforts to extend these cohesive models to fully three-dimensional problems have been made by Ortiz and co-workers[11,12]. Thereafter, similar works have found this tool to be highly predictable of different kinds of three-dimensional problems[13,24]. However, there is a set of problems involving thin-walled structures (such as the analysis of thin plates, fuselage, sheet-metal forming, crashworthiness) where the use of 3D solid elements would be prohibitive from the computational viewpoint. Generally, these engineering problems are solved with shell or other structural elements[14]. Li and Siegmund[15] made the first attempt to extend the cohesive zone model for shell elements. In their work, crack propagation under mode I/III conditions was studied in aluminum panels. However, the out-of-plane bending deformation was not contemplated in their cohesive model. It should be mentioned that, although the extension of the three dimension cases is relatively simple, shell elements present the challenge of having additional degree of freedom (i.e. nodal rotations), which may help to identify other failure modes, such as surface crack propagating through the thickness of shell under bending conditions.

In this work, the cohesive interface model is extended to handle cracks in the context of three-dimensional shell elements. In addition to the traction-displacement law, a bending moment-rotation relation is included to transmit the moment and describe the initiation and propagation of cracks growing through the thickness of the shell elements. The paper is organized as follows: The description of the interface cohesive element and the constitutive law is given in section 2. Simulations of simple Mode I/III crack propagation problems and bending configuration in a thin elastic plate are discussed in section 3. A study of ductile crack propagation of elasto-plastic material, and how this affects the determination of the cohesive parameters is included in Section 4. To conclude, the effect of plate thickness into the three-dimensional plastic constrain that affects crack growth is discussed in section 4.1. A

simple technique is suggested for defining a constitutive cohesive law compatible with two-dimensional nature of shell model.

2 MODEL DESCRIPTION

2.1 Interface Elements for Shell Elements

The description for the formulation of the interface cohesive element for shell elements is based on the zero thickness 4-noded linear interface element described in previous works[6,7] extended to 3-D *"line"* interface elements connecting two quadrilateral shell elements. These interface elements are embedded along shell element boundaries as indicated in Figure 1(a).

The model assumes that a perfect interface between two surfaces carries forces that oppose separation and shear between them until decohesion. From that point, the two surfaces will behave as distinct entities. The propagation of a crack can thus be simulated as the consecutive failure of interface elements. The cohesive relationship is expressed in terms of the opening displacement $\Delta = \{u_n, u_{t1}, u_{t2}\}^T$ and the traction $\mathbf{T} = \{T_n, T_{t1}, T_{t2}\}^T$, where the subscripts *n*, *t1* and *t2* denote the component of the traction and displacement in the direction of the local axes of coordinates. The magnitude of the opposing forces before debonding is a function of the relative normal and shear displacement jumps between the two surfaces, and this relationship is given by the constitutive cohesive law, $\mathbf{T} = f(\Delta)$. The interface between two shell elements is "intact" until the interface traction reaches a maximum value $T_{max,}$ and reduces to zero until the displacement jump reaches the maximum value. The reduction of cohesive traction can be interpreted as the progressive degradation of an otherwise intact stress state ahead of the crack tip. Details of the constitutive cohesive laws will be given in the next section.

This shell interface element should be compatible with the formulation of the shell element. In this work, the Belytschko-Lin-Tsay shell element[16] is considered. This shell element, which is the default shell element implemented in explicit finite element software DYNA3D[17], is widely used in several applications including crashworthiness and structural analysis. The formulation of this shell element uses the Mindlin theory of plates[18], which allows for transverse shear strains through the thickness of the plate. Since the displacements in a quadrilateral shell element can be approximated with classical C^0 interpolations, each node has six degrees of freedom, three translational, (*x*, *y*, *z*) and three rotational, ($\theta_x, \theta_y, \theta_z$). As shown in Figure 1(a) the geometrical description of the interface element is only given by the nodal position.

2.2 Constitutive Cohesive Law

In this work, the so-called *triangular law* introduced by Espinosa and Zavattieri[6,7] is extended to 3-D interface elements connecting quadrilateral shell elements. In formulating the cohesive law, a non-dimensional effective displacement jump is defined by $\lambda = \sqrt{(u_n/\delta_n)^2 + \beta_2^2 (u_{t1}/\delta_{t1})^2 + \beta_2^2 (u_{t2}/\delta_{t2})^2}$, where u_n, u_{t1} and u_{t2} are the actual normal

and tangential displacement jumps at the interface estimated by the finite element analysis, and δ_n, δ_{t1} and δ_{t2} are the critical values at which the interface failure takes place.

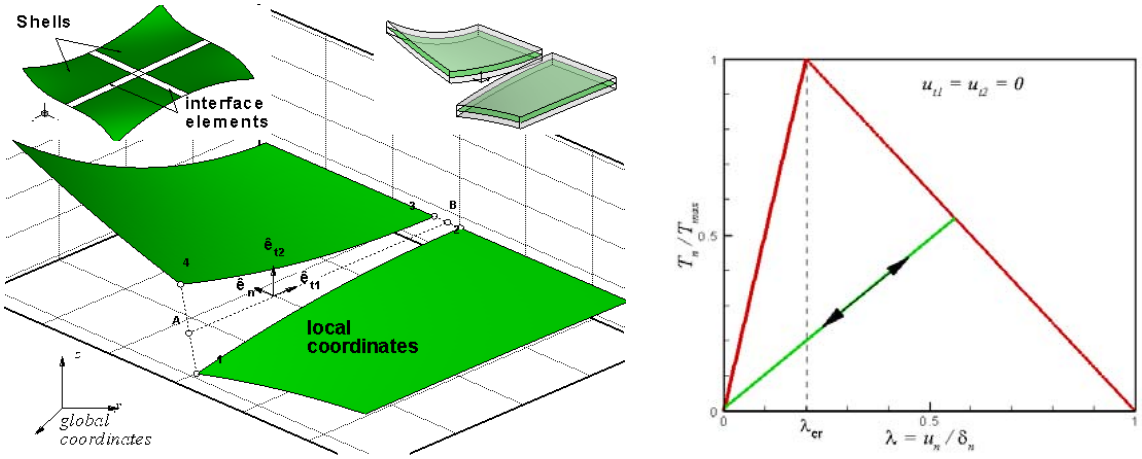

(a) (b)

Figure 1: (a) Schematics of the separation between two shell elements. The local coordinates are defined in the middle line of the interface elements. The upper-left box shows the cohesive interface elements embedded along quadrilateral shell elements (For illustration purposes, the shell elements have been separated). (b) Traction separation law for pure normal separation. The arrows indicate unloading and loading for $\lambda > \lambda_{cr}$.

Assuming a potential of the form $\Phi(u_n, u_{t1}, u_{t1}) = \delta_n T_{\max}\left(\lambda - \lambda^2/2\right)/\left(1-\lambda_{cr}\right)$, then the components of the traction acting on the interface in the fracture process zone in the local configuration are given by

$$
\begin{aligned}
T_n &= \frac{\partial \Phi}{\partial u_n} = \frac{\partial \Phi}{\partial \lambda}\frac{\partial \lambda}{\partial u_n} = \frac{1-\lambda}{\lambda}\left(\frac{u_n}{\delta_n}\right)\frac{T_{\max}}{\left(1-\lambda_{cr}\right)} \\
T_{t1} &= \frac{\partial \Phi}{\partial u_{t1}} = \frac{\partial \Phi}{\partial \lambda}\frac{\partial \lambda}{\partial u_{t1}} = \frac{1-\lambda}{\lambda}\left(\frac{u_{t1}}{\delta_{t1}}\right)\frac{\alpha_1 T_{\max}}{\left(1-\lambda_{cr}\right)} \\
T_{t2} &= \frac{\partial \Phi}{\partial u_{t2}} = \frac{\partial \Phi}{\partial \lambda}\frac{\partial \lambda}{\partial u_{t2}} = \frac{1-\lambda}{\lambda}\left(\frac{u_{t2}}{\delta_{t2}}\right)\frac{\alpha_2 T_{\max}}{\left(1-\lambda_{cr}\right)}
\end{aligned}
\qquad (1)
$$

where $\alpha_1 = \beta_1^2(\delta_n/\delta_{t1})$ and $\alpha_2 = \beta_2^2(\delta_n/\delta_{t2})$. λ is monotonically increasing and has the form $\lambda = \max\left(\lambda_{\max}, \lambda\right)$ with $\lambda_{\max} = \lambda_{cr}$ at the beginning. Once the maximum traction is reached, the interface starts failing and the traction reduces to zero up to the maximum displacement jump, and any unloading in the range $\lambda_{cr} < \lambda \le 1$ takes place irreversibly. Once the effective displacement jump, λ, reaches or exceeds a value of 1, the interface element is

broken and the crack is said to have initiated. Subsequent failure of neighboring interface elements leads to crack evolution. The most attractive feature of this new law is that this irreversible behavior is already incorporated in the law. Figure 1(b) shows the variation of the tensile cohesive traction $T_n / T_{\max}$ with respect to the non-dimensional normal and tangential displacement. The area under the curve for normal traction in the absence of tangential traction gives the critical strain energy release rate G_{Ic} for Mode I, namely $G_{Ic} = \delta_n T_{\max} / 2$. Similarly, the energies for Mode II and III can be obtained as $G_{IIc} = \beta_1^2 G_{Ic}$ and $G_{IIIc} = \beta_2^2 G_{Ic}$, respectively. Once $\lambda \geq \lambda_{cr}$ the cohesive interface begins to dissipate irreversible energy defined as $G_{dis} = G_{Ic}(\lambda_{\max} - \lambda_{cr})/(1-\lambda_{cr})$.

2.3 Fracture by bending

In this section, a novel cohesive formulation that accounts for the effect of cracks growing through the thickness by bending is proposed. In addition to the traction-displacement law (Equation 1), a bending moment-rotation relation is included to transmit the moment and describe the initiation and evolution of cracks. In formulating this cohesive law, a non-dimensional effective displacement jump is redefined by adding an extra term, $\lambda = \sqrt{(u_n/\delta_n)^2 + \beta_2^2 (u_{t1}/\delta_{t1})^2 + \beta_2^2 (u_{t2}/\delta_{t2})^2 + \hat{\beta}^2 (\Delta\theta/\Delta\theta_{\max})^2}$. Since cracks are allowed to grow along interface elements, and assuming that the crack will grow in the direction of the maximum stress produced by bending, only the rotation θ_{t1} in the direction $\hat{\mathbf{e}}_{t1}$ (parallel to the middle line) will be considered.

Assuming the same potential of section 2.2, the expressions of the normal and tangential tractions remain the same as in Equation (1), except that λ has a contribution from the rotation; and the bending momentum is given by

$$M_{t1} = \frac{\partial \Phi}{\partial \Delta\theta} = \frac{\partial \Phi}{\partial \lambda}\frac{\partial \lambda}{\partial \Delta\theta} = \frac{1-\lambda}{\lambda}\left(\frac{\Delta\theta}{\Delta\theta_{\max}}\right)\frac{\hat{\alpha} T_{\max}}{(1-\lambda_{cr})} \tag{2}$$

where $\hat{\alpha} = \hat{\beta}^2 (\delta_n / \Delta\theta_{\max})$. Since $\hat{\beta}$ is non-dimensional, $\hat{\alpha}$ has dimensions of length/radians and a maximum momentum can be defined as $M_{\max} = \hat{\alpha} T_{\max}$. If only pure rotation along the axis $\hat{\mathbf{e}}_{t1}$, this bending moment-rotation relationship represents a non-linear rotational spring carrying a momentum that opposes the bending. Under theses circumstances, the cohesive law has the same triangular shape as the one shown in Figure 1(b). The rising portion of the curve correspond an intact shell and any loading/unloading takes place linearly with an initial bending stiffness given by $\kappa = M_{\max}/(\lambda_{cr} \Delta\theta_{\max})$. When the bending momentum reaches a maximum value $M_{\max}$ a surface crack initiates and propagates through the thickness. Any unloading in the range $\lambda = [\lambda_{cr}, 1]$ will take irreversibly with a bending stiffness lower than the initial value. That bending stiffness will decrease as the crack grows

until the interface element *breaks* at $\lambda = 1$.

In early works, the concept of including a rotational spring along shell element boundaries has been introduced by Rice and Levy[19] and later extended to stationary elastic-plastic crack analysis by Parks and White[20]. In their work, the spring represents the additional compliance contributed by the presence of stationary part-through surface cracks. In this new model the same idea is applied in the context of the cohesive zone model, allowing the crack to propagate due to the bending moment and in-plane stresses.

3 CRACK PROPAGATION IN ELASTIC THIN PANNELS

In this section, we will present a simple case of crack propagation in a pre-cracked elastic thin panel under three different loading conditions: tension, torsion and bending. The main purpose of this study is to compare the new cohesive model for shells with a fully three-dimensional model based on hexahedral continuum elements an their respective cohesive interface elements. Considering that the cohesive zone model has been successful tested for solid elements in two and three dimensions[3-13], this comparison will allow us to determine how well the proposed model for shell elements is capable to predict the same fracture behavior using less computational time.

As shown in Figure 2(a), the length of this panel is $L = 30\ cm$, the width $W = 12.7\ cm$ and thickness $t = 6\ mm$. The tensile axis is aligned with the y-direction and a crack of initial length $a_0 = 26\ mm$ lies along the line $y = 0$. For all the cases, the specimen is simulated using both hexahedral and shell meshes. The hexahedral mesh has been constructed using the same shell elements as base with four hexahedral elements through the thickness. The shell element selected is the Belytschko-Tsay shell with five integration points through the thickness. In this analysis, cohesive interface elements are only embedded along the line y = 0, so that the crack is constrained to grow along the initial crack line. Since the material used for these simulations (Steel C300) behaves in a brittle fashion, it is assumed that the crack will only grow under pure mode I and crack branching is not allowed. It should be mentioned that this kind of assumption is commonly used for several investigators[4,11,12,15]. The constitutive material parameters for steel C300 are: $E = 200\ GPa$, $\nu = 0.3$, $\rho = 7830\ kg/m^3$. The cohesive parameters are: $T_{max} = 700\ MPa$, $\delta_n = \delta_{t1} = \delta_{t2} = 70\ \mu m$, $\beta_1 = \beta_2 = 1.0$ and $\lambda_{cr} = 0.3$. In addition to the condition that the element size has to be much smaller than the dimension of the block to provide an accurate resolution of the stress near the crack tip, the cohesive element size should be also able to resolve the cohesive zone length. Given the material parameters, the cohesive zone length is $l_{cz} \approx 20\ mm$[5-7]. Therefore to satisfy all the length scales a cohesive element size of approximately $L_e = 1\ mm$ was chosen. In this preliminary study, the material is treated as elastic, using the continuum elastic model for large deformations available in Dyna3D[17]. Discussion on elastic-plastic material is given in Section 4.

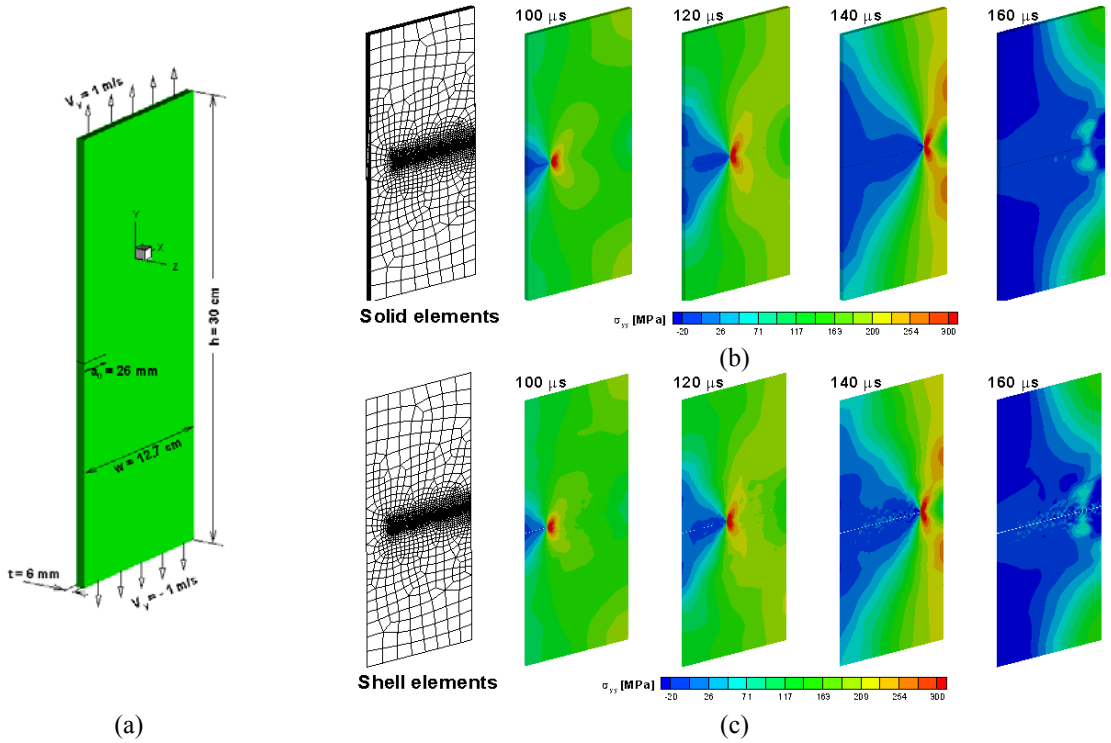

Figure 2: (a) Geometry and boundary conditions for the tensile test of the pre-cracked plate (b) Hexahedral mesh. (c) Shell mesh. Tensile stress σ_{yy} at different times during the propagation of the crack using a shell mesh.

Cohesive interface elements connecting hexahedral elements: Similar to the case of shell elements, the formulation of the cohesive interface elements connecting the faces of two hexahedral elements is based on a zero-thickness 8-noded quadrilateral *"plane"* elements. Like in any traditional cohesive interface element for 2- and 3-D only the displacement-traction relationship constitute the cohesive law[3-7,11-13]. The components of the opening displacement are $\Delta = \{u_n, u_{t1}, u_{t2}\}^T$, and the non-dimensional effective displacement jump becomes $\lambda = [(u_n/\delta_n)^2 + \beta_2^2(u_t/\delta_t)^2]^{1/2}$ where $(u_t/\delta_t)^2 = (u_{t1}/\delta_{t1})^2 + (u_{t2}/\delta_{t2})^2$. As a result, the cohesive law employed for these interface elements is the same as the one given by Equation 1 considering $\delta_{t1} = \delta_{t2} = \delta_t$. The main difference between this cohesive law and the one proposed for the shell interface element in section 2.1 is that it is not necessary to make any difference between the tangential components.

3.1 Mode I crack propagation: Tension test

In this case the rectangular thin-walled specimen is subjected to dynamic tensile loading on both, upper and bottom boundaries given by a uniformly applied velocity at the top and bottom boundaries, $v_y = \pm 1$ *m/s* as shown in Figure 2(a). The simulations were carried out for 200 microseconds until the crack reaches the other end of the plate. Figure 2 shows the

tensile stress σ_{yy} at the point where the crack starts to propagate. The contours show identical stress distribution for both cases. Figure 2 (a) and (b) show the evolution of the tensile stress σ_{yy} when the crack propagates from side to side for the fully three-dimensional model and shell model at identical times, respectively. The close agreement between both simulations indicates that this problem is suitable to be treated with shells. In order to verify the validity of these results, two more simulations have been performed at different loading rates. Figure 3(a) shows the crack tip position as function of the applied displacement for v_y = *0.1, 1* and *5 m/s*. The crack tip position is determined by the global position of the integration point in which the condition $\lambda = 1$ is satisfied. Figure 3(b) shows the normal force for the three loading rates. In these figures the solid line represent the simulations with solids and the dashed line the simulations with shells. It is clear from these results that both models can predict exactly the same the material response.

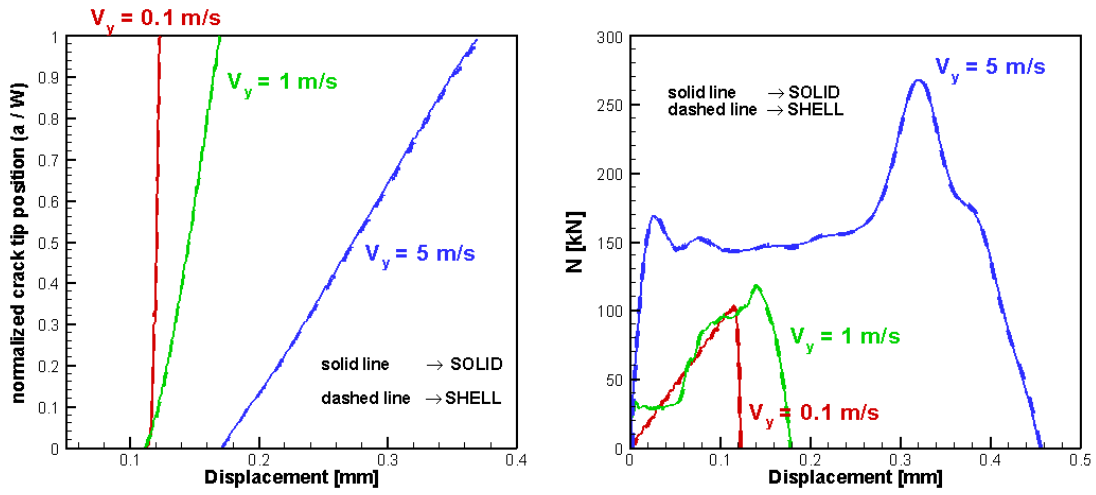

(a) (b)

Figure 3: (a) Crack tip position vs displacement for three different loading rates. (b) Normal force vs displacement for three different loading rates.

3.2 Mode III crack propagation: Torsion test

To further test the model, the same specimen is simulated with solid and shell elements under torsion load. As in previous case, the boundary conditions are only applied on the top and bottom boundaries, except that in this case a constant rotational velocity field of $\dot{\theta} = 0.08$ *rad/sec* is applied. This geometry and loading conditions creates a mode III stress field near the crack trip/front. As in previous case, the loading conditions and cohesive parameters are similar for both models. Given the asymmetric conditions at the crack plane, the moment-rotation relationship does not play an important role yet. However, this problem complements in some way the one considering only pure mode I. The results of these simulations are depicted in Figure 4. The crack tip position as function of time is similar for both cases. The

tensile stress σ_{yy} when the crack front reaches the middle of the plate is shown for both cases in Figure 4(b). Although the stress fields look different for both cases, the reader should note that the stress in the shell elements is given in the middle plane as opposed to the solid case where the visualized stress field corresponds to the surface. A closer examination of the middle plane in the solid case revealed that the stress field is similar to the one with shell elements (Figure 4(b) and (c)).

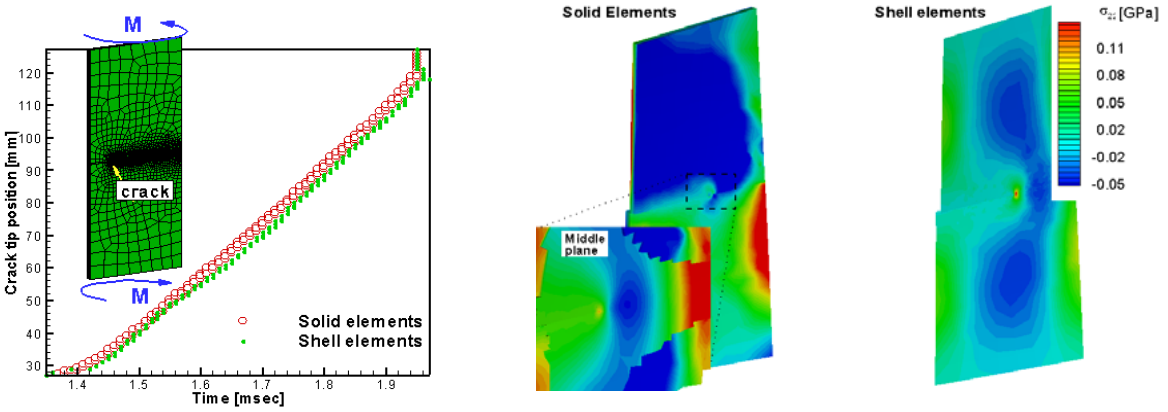

(a) (b) (c)

Figure 4: (a) Crack tip position as a function of time for the case where the elastic thin plate is loaded under dynamic torsion. (b) Stress σ_{yy} distribution for the case modeled with solid elements at 1.7 msec.The window in the lower-left corner is cross-section of the middle plane at *z=0*. (c) Stress field for the case simulated with shell elements. Note that the stress in the case with shells is given in the middle plane.

3.3 Bending test

In this case, the same pre-cracked plate is loaded in a three-point bending setup. Unlike, traditional setups to study crack propagation, in this specific problem the applied load is perpendicular to the plane of the plate such that out-of-plane bending is induced. The main idea behind this test is to provoke through-the-thickness crack propagation. The layout of this experiment is shown in Figure 5(a). Two cylindrical rods are positioned under the plate, each one at *10 cm* from crack plane. A third rod aligned with the crack plane is positioned just above the plate and it moves towards the plane with a constant velocity $v_z = 1$ *m/s*. The diameter of the rods is *1 cm*. It was observed that one of the advantages of this setup is that the crack front propagates in two directions: (1) perpendicular to the plane of the plate, along the *z-axis* from the top to the bottom (through-the-thickness crack propagation) and (2) in the direction of the original crack along the *x-axis*, from the initial crack front to the other side of the plate. This leads to a more controlled crack growth, as opposed to the case without initial crack where the crack can grow through the thickness in an unrestrained mode. Although, the shell model is not able to explicitly predict through-the-thickness crack growth, this configuration will test the capability of the model to predict the overall response of the structure.

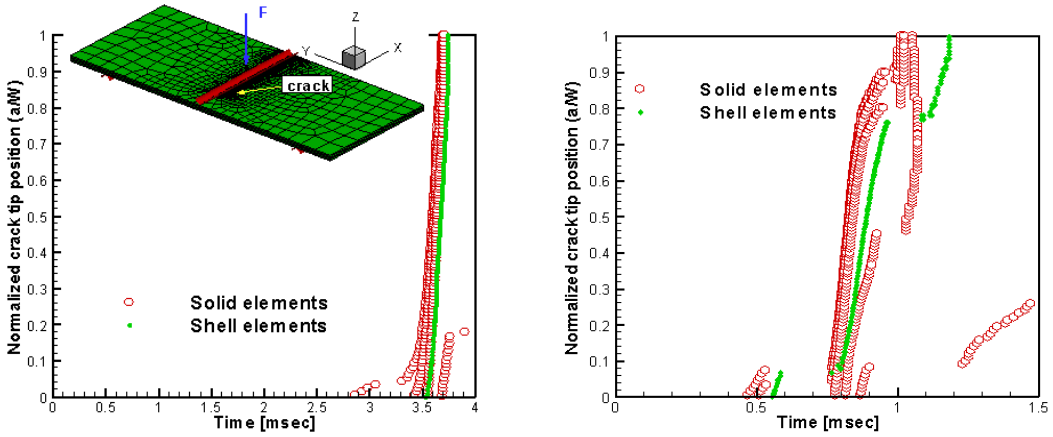

Figure 5: Schematics of the three-point bending setup. (a) Crack tip position as a function of time for case with thickness *t=6 mm* and v_z *= 1m/s* (b) Crack tip position as a function of time for case with thickness *t=2 mm* and v_z *= 10 m/s*

As in previous cases, the cohesive parameters used for the shell model are the same as those used in the fully three-dimensional case. However, in this case the moment-rotation relationship of Equation 2 becomes an important part of the overall constitutive cohesive law and, therefore, the cohesive parameters $\Delta\theta_{\max}$ and $\hat{\beta}$ need to be determined. Several simulations were performed with different parameters until good match was achieved. Figure 5(a) shows the crack tip position as function of time for best case with $\Delta\theta_{\max} = 0.05\,rad$ and $\hat{\beta}$*=1.0*. In this figure, the crack evolution is represented by the x-coordinate of the integration points of the interface elements at the time where $\lambda = 1$ is satisfied. In the simulation with solid elements (red circles), several integration point have the same *x*-coordinate, however the time where the crack front passes through those points may be different. This confirms that the crack grows in two directions along the projected crack plane. Furthermore, it was observed that the crack initiates originally at the intersection of the initial crack front and the bottom surface and propagates to the upper surface as it grows in the *x*-direction.

A second configuration is tested to validate the model parameters. The thickness of the plate is reduced to 2 mm, and the impact velocity is increased to v_z *= 10 m/s*. The crack tip position as a function of time is shown in Figure 5(b). Although the fully three-dimensional simulation case shows a strong through-the-thickness crack propagation the shell model is able to predict the crack propagation in the *x*-direction. Moreover, it is observed that the overall force needed in the upper rod to break the plate is similar using both models. The bottom view of the cracked plate and the stress field are shown in Figure 6 for both models at three different times where the crack growth takes place. The position of the crack front/tip can be estimated from the stress field. It should be noted that the stress shown in the simulation with solid elements is that of the bottom surface of the plate, whereas the one

shown in the case with shells represents the middle plane stress field. Therefore, the crack tip position of the model with shells as described in Figure 5 can be considered as the position of the crack front at the middle plane.

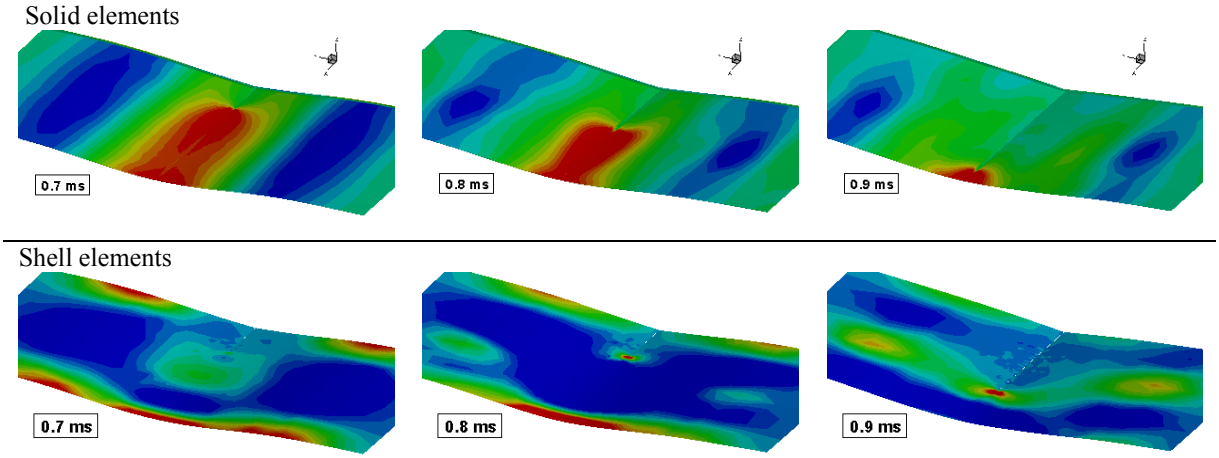

Figure 6: Tensile stress σ_{yy} at different times during the propagation of the crack using a shell and solid mesh for the three-point bending configuration for $t = 2mm$ and $v_z = 10\ m/s$.

4 THREE-DIMENSIONAL EFFECTS OF DUCTILE CRACK PROPAGATION IN THIN-WALLED SPECIMENS

The potential of the cohesive zone model to simulate crack propagation in elastic thin plates using shell elements has been examined in the last section. The material under consideration was only elastic, and in most cases the crack front was straight. Consequently, the plane stress formulation used by the shell elements may be suitable to model these kinds of problems. However, this desired behavior might not be observed in real ductile materials. The study of ductile fracture in elasto-plastic materials raises some concerns regarding the mechanical constraint imposed by the plastic deformation in the region near the crack front. Moreover, during ductile crack propagation of thin metals, a characteristic phenomenon called crack tunneling is observed. Crack tunneling is when the initially straight crack front grows more rapidly in the middle of the thin-walled specimen leading to the formation of rounded crack front profile. The plastic deformation around the tunneled crack front departure from the ideal deformational state observed in the elastic cases. As a consequence, additional out-of-plane components of shear stress become significant as the highly plastic deformation takes place near the crack region. In addition to crack tunneling, slant crack growth could also occur in certain conditions and materials. This is when the crack front turns into a 45^o direction leading to a mixed mode I/III crack growth problem[21]. The study of slant fracture and its transition from flat crack is out of the scope of this analysis. Thus, we will restrict the current study to problems where crack fronts advance in flat mode.

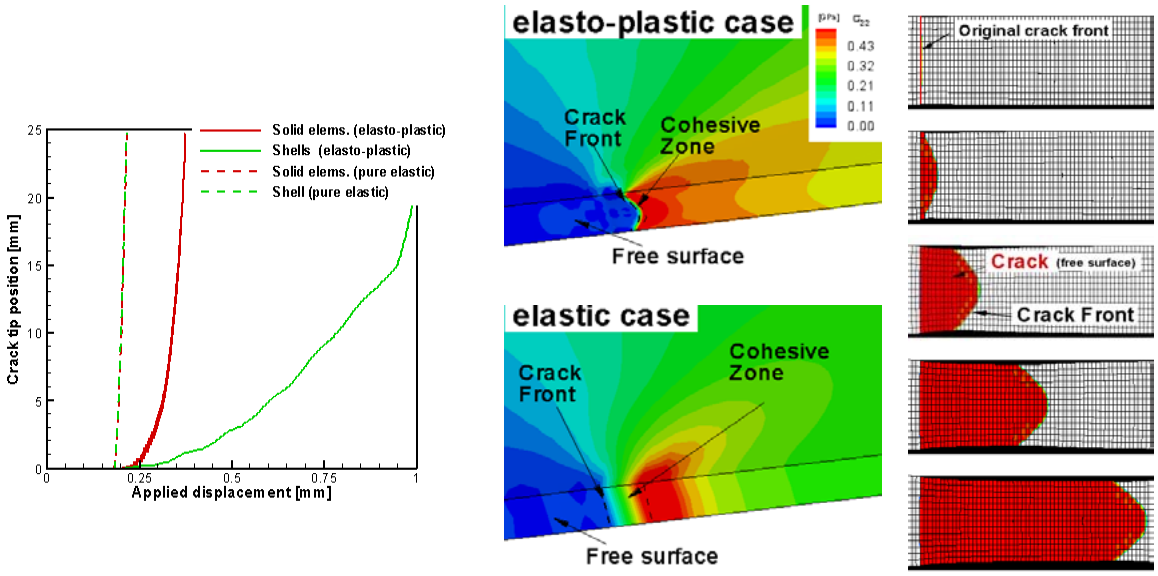

(a) (b) (c)

Figure 7: (a) Crack tip position as function of the applied displacement for a mode I ductile crack problem simulated with solid and shell elements. The dashed lines indicate the solution when the material is treated as pure elastic. (b) Tensile stress field for the elasto-plastic and elastic material. (c)Details of the crack tunneling for the case modeled with 3d solid elements. The red region indicates where $G_{dis} / G_{Ic} = 1.0$.

To illustrate the importance of the three-dimensional effect of tunneling in the crack region, an elasto-plastic specimen loaded in mode I is simulated with solid and shell elements. Details of this setup and material model are given later in section 4.1. The same configuration is simulated with a pure elastic model for comparison purposes; however, the cohesive parameters are the same for all these simulations. Figure 7(a) compares the crack tip position as a function of the applied displacement for all these cases. Even though there is an excellent agreement when the material is elastic (as observed in section 3.1), a noticeable disagreement in crack growth between the solid and shell model is obtained for the elasto-plastic case. Based on the hypothesis that the three-dimensional simulation contains the most reliable information about the true deformation process, there is clearly something missing in the model for shells. The three-dimensional tensile stress fields (σ_{yy}) for the elasto-plastic and pure elastic case are shown in Figure 7(b). For illustration purposes, only one half of the specimen from the crack plane is shown. The presence of a more complex three-dimensional stress state ahead of the crack front is evident in the elasto-plastic case. The same figure indicates the location of the crack front and the cohesive zone defined as the region where irreversible energy dissipation takes place $0 \le (G_{dis} / G_{Ic}) < 1$ (see section 2.2). Although not shown in this paper, it is also observed the formation of *"shear lips"* caused by the plastic deformation on the free borders. Figure 7(c) shows the predicted crack front formation at different stages. The initial straight crack front evolves into a round-shaped crack front. The

red region indicates where the material has been totally separated (where $G_{dis}/G_{Ic}=1.0$). A thick black line on the free surfaces depicts evidence of thickness reduction.

Unfortunately, the localized three-dimensional deformational state near the crack front affects the overall response of the structure; and the bi-dimensional nature of the plane stress formulation is evidently not adequate to capture this phenomenon[22]. Nevertheless, it may still possible to *"lump"* this localized behavior into the cohesive zone model. In this section, we will study this alternative by explicitly modifying the existing constitutive cohesive law to incorporate some geometrical and material factors that would eventually take into account the complexity of the tunneling effect. As an example, a mode I crack propagation experiment performed by Doods and co-workers[23] on constrained center-cracked aluminum panel specimens will be used. It should be mentioned that, even though this experiment has been modeled with the cohesive zone model using both solid elements (Roychowdhury et al.[24]) and shell elements (Li and Siegmund[15]), both papers have reported different values of cohesive strength. This discrepancy will be discussed later in the section.

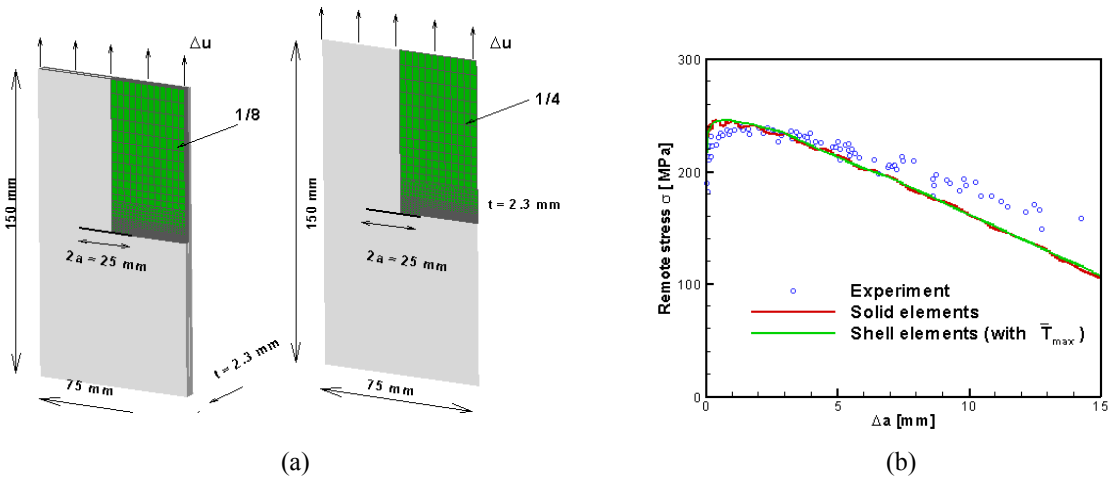

(a) (b)

Figure 8: (a) Details of the center-cracked aluminum panel. For simplicity, the solid model considers only one-eight of the geometry, and the shell model one-fourth. Symmetry boundary conditions are applied accordingly. (b) Predicted and measured load-crack growth response using both models.

4.1 Analysis of a center-cracked aluminum panel

Following the work by Doods and co-workers[23,24], simulations of an aluminum Al2024-T3 centered-crack panel are performed with the fully three-dimensional model. As described in Figure 8(a) the width of the panel is $2w = 75\ mm$. The initial crack length is $a/w = 0.333$ and the thickness of the plates is $t = 2.3\ mm$. Due to the symmetry of this configuration only one-eight of the geometry is simulated. Thus, symmetry boundary conditions are employed accordingly. Cohesive elements are inserted in the projected crack plane/line. The element size in the fracture region is $L_e = 0.1\ mm$ in the crack direction and $L_t = 0.16\ mm$ in the thickness direction. This provides seven layers of elements across half-thickness. Mesh

convergence studied performed by Doods[24] demonstrated that this is sufficient refinement to capture proper crack growth and tunneling formation. In order to simulate the quasi-static test with displacement control loading using an explicit code such as Dyna3D, uniform low velocities are applied at the nodes on the top boundary. Previous calculations demonstrated that applied nodal velocities of about *500 – 750 mm/sec* are slow enough to prevent inertia effects in the calculation and satisfactorily fast to improve CPU efficiency. For the continuum material, the traditional isotropic elastic-plastic constitutive model that uses the Mises yield criterion is utilized. The elastic parameters for the Al2024-T3 are $E = 71.3\,GPa$ and $\nu = 0.3$. The initial yield stress is $\sigma_y = 345\,MPa$ and the plastic regimen is governed by $\sigma = \mathbf{K}\varepsilon^n$, where $\mathbf{K} = \sigma_y (E/\sigma_y)^n$, $n = 0.1$ is the hardening exponent, σ is the true effective stress and ε is the logarithmic strain. Due to the localized high plastic deformation ahead of the crack front, fully integrated 8-noded solid elements (hexahedral/brick) are used. The cohesive elements are also fully integrated for compatibility. A systematic and parametric study performed by Roychowdhury et al.[24] led to the following calibrated cohesive parameters: $T_{\max} = 2.7 \cdot \sigma_y = 931.5\,MPa$ and $G_{Ic} = 19\,kJ/m^2$ (equivalent to a material toughness of $K_{Ic} = 38.5\,MPa\sqrt{m}$). Figure 8(b) shows a good agreement between the numerical predictions and the experimental load-crack extension data. The simulation with shells will be discussed later.

Simulation with shell elements: Following the same scheme, the specimen is simulated with quadrilateral shell elements. In this case only one-quarter of the geometry is modeled with shells. As shown in Figure 8(a), the shell mesh utilized is identical to one of the faces of the fully three-dimensional case. Keeping the same element size, the number of elements is therefore reduced from 21,700 solid elements and 1,750 *plane* cohesive elements to only 3,500 shell elements and 250 *line* cohesive elements. However, results using the same cohesive parameters as those used in the three-dimensional case are markedly different. Crack propagation is slower than in the real case and the applied peak force is significantly over predicted. Figure 9(a) shows the crack extension and normal applied force for the three-dimensional case (dashed line) and the shell simulation (orange solid line). The same effect has been observed in later simulations with specimens of different thicknesses. Interestingly, the fully three-dimensional simulations show a strong dependency of the overall material behavior with the specimen thickness, whereas the shell model predicts the same behavior; that is the remote applied stress and crack extension are independent of the specimen thickness. It is clear that the cohesive law needs to be modified in order to take into account the three-dimensional effect that the shell elements cannot provide.

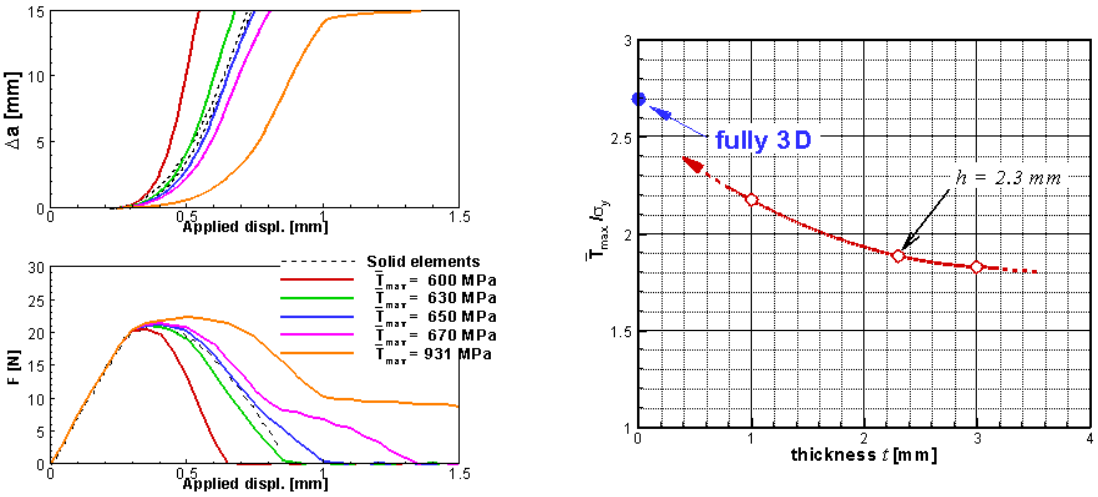

(a) (b)

Figure 9: (a) Crack extension and force as a function of the uniformly applied displacement obtained with the fully-three-dimensional model (black dashed lines) and with the shell model using different cohesive strength values (all solid lines). The two dashed lines indicate the crack front position at the middle and outer surface of the specimen with thickness $t = 2.3mm$ (b) Correction of the cohesive strength for shell elements as a function of the specimen thickness.

Calibration of the shell model: As mentioned before, Li and Siegmund[15] demonstrated that the cohesive zone model could certainly be used with shell elements to model these kinds of problems. Nevertheless, they reported a much lower value for the cohesive strength ($\overline{T}_{\max} = 2\sigma_y$). Prior works on dynamic crack growth in thin sheets also lead to similar findings[25]. This indicates that possible modifications of the cohesive zone model can involve a reduction of the cohesive strength. However, to the best of the author's knowledge, there is no work done on defining some sort of scaling law to relate the "true" cohesive strength, $T_{\max}$ (in this case, the one used for the three-dimensional calculations) with the "modified" cohesive strength, $\overline{T}_{\max}$ for a 2D formulation. It is believed that the true cohesive strength used in 3D simulations is intrinsic of the material and should not change with geometry or loading conditions. On the other hand, the modified cohesive strength for shell elements should eventually contain information of the geometry.

Looking at this trend, a series of numerical simulations with shell elements was performed for various values of the cohesive strength, $\overline{T}_{\max}$ and keeping the same cohesive energy G_{Ic} (the critical displacement is then computed as $\delta_n = 2G_{Ic} / \overline{T}_{\max}$). Figure 9(a) shows the crack extension and force as a function of the remote applied displacement for different values of $\overline{T}_{\max}$ using the shell model (solid lines). It is observed that crack grow is delayed for higher values of $\overline{T}_{\max}$. Conversely, the peak force increases with $\overline{T}_{\max}$. In conclusion, it was found that, with $\overline{T}_{\max} = 1.88 \cdot \sigma_y = 650\,MPa$, the shell model gives similar results to the three-

dimensional model. The force-crack extension curve was also included in Figure 8(b) for comparison purposes. This value is closer to Li and Siegmund's findings[15].

Certainly this change in the value of $\overline{T}_{\max}$ is an "ad-hoc" modification of the cohesive law to take into account the three-dimensional effects for this specific thickness and material; hence, it should be expected that this correction would be different for other thicknesses or material (different values of E, ν, σ_y, n). Therefore, two more three-dimensional simulations were added for two more thicknesses, *t = 1* and *3 mm* using the "intrinsic" cohesive parameters $T_{\max} = 931.5 GPa$ and $G_{Ic} = 19 kJ/m^2$. Then, the same process was repeated for these two new specimens. Again, simulations with the shell model were performed for different values of $\overline{T}_{\max}$ for the two cases until good agreement was achieved. Finally, the best match was attained with $\overline{T}_{\max} = 2.17 \cdot \sigma_y$ for *t = 1 mm*, and $\overline{T}_{\max} = 1.28 \cdot \sigma_y$ for *t = 3 mm*. Figure 9(b) shows the best match $\overline{T}_{\max}$ versus the specimen thickness. This clearly demonstrate that the cohesive model for shell elements is affected by the geometry, at least for the modeling of cracks under normal opening,

It should be mentioned that, although it is common practice to report only the force versus crack extension curves for these kinds of experiments (Fig. 8(b)); the individual evolutions of these two variables with respect to the applied remote displacement (Fig. 9(a)) are more sensitive to the cohesive parameters than just the combination of the two. Therefore, the two curves should be used simultaneously for calibration and validation purposes.

"Effective" cohesive law: Another way to look at this problem is by analyzing in details the three-dimensional deformational state and extract from the calculations useful information that can eventually provide some guidelines to define a cohesive law for shell elements. Thus, it can then be possible to look at the bi-dimensional solution as a projection of the three-dimensional case. For instance, the three-dimensional cohesive zone ahead of the mode-I crack front, defined by the normal cohesive traction, is shown in Figure 10(a-upper corner). The maximum traction (when $T_n = T_{\max}$) follows a curved shape similar to the tunneled crack front. The same figure shows the profile of the normal traction along the *x*-axis in the direction of the crack growth. Data points represent the normal traction at each integration points of the three-dimensional calculation. The average *through-the-thickness* cohesive traction can be easily obtained by $\overline{T}_n = 2/t' \int_0^{t'/2} T_n dz$ (shown as red dashed line), where *t'=t'(x)* is the current thickness. The averaged maximum traction is then defined as $\overline{T}_{\max}$,which is notably lower than the intrinsic cohesive strength. It was observed that this profile, as well as $\overline{T}_{\max}$, remains constant as the tunneling is fully developed and cracks propagate steadily. Three-dimensional simulations of different thicknesses reveal that this averaged maximum traction decreases for thicker panels.

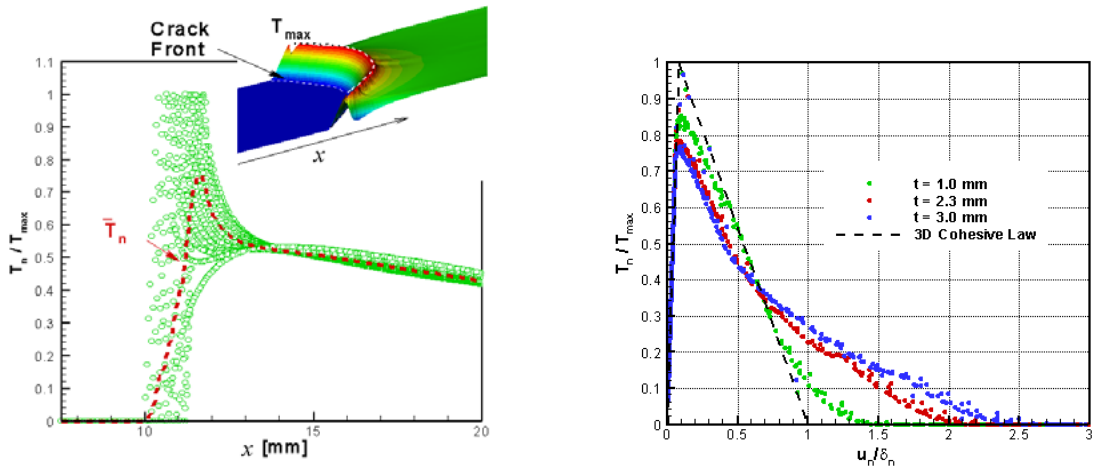

(a) (b)

Figure 10: (a) Normal cohesive traction profile developed near the crack front. Each green dot represents the value at each integration point and its x-coordinate (initial straight crack front is located at *x=0*). The dashed red line represents its average through the thickness $\overline{T}_n$. (b) Effective cohesive law ($\overline{T}_n$ vs. $\overline{u}_n$) for three different specimen thicknesses.

Conversely, the opposite effect was found with the averaged normal opening (defined as $\overline{u}_n = 2/t' \int_0^{t'/2} u_n dz$), in which the averaged maximum critical displacement is greater than the intrinsic one and increases with the thickness of the panel. More remarkable is the combination of these two variables. Figure 10(b) shows the relationship between $\overline{T}_n$ and $\overline{u}_n$. Each dot represents the values at integration points of the plane cohesive elements at various stages of the crack propagation simulation. This well-defined "effective" cohesive law is shown for three thicknesses *t = 1, 2.3* and *3 mm*. The original cohesive law ($T_{\max} = 931.5\,MPa$ and $G_{Ic} = 19\,kJ/m^2$) is also shown in dashed lines. Even though the shape of the cohesive laws departs from the original triangular shape, the overall cohesive energy does not deviate significantly from its original value, which confirms the assumption used in the previous section of keeping the same energy and only modifying the cohesive strength. In all the cases, the initial stiffness also remains unchanged. Consequently, these cohesive laws have been implemented for shell elements, and simulations for each thickness were performed. Although, a similar trend to that described in previous section was observed, the crack extension and applied force were not as accurate as the results obtained with the "calibrated" cohesive parameters. One possible explanation is that the averaged cohesive are slightly greater than those obtained in the calibration process and, hence, do not take into consideration the real three-dimensional character of crack growth by only projecting in a 2D plane. However, this "effective" cohesive law provides some qualitative insight into the real mechanisms that need to be applied in order to define cohesive laws that can be compatible with a plane stress formulation.

5 CONCLUSIONS

In this paper, a three-dimensional finite-deformation cohesive element for shell elements for the finite element analysis of crack propagation in thin-walled structures was presented. A numerical analysis for elastic thin plates was included to assess the capability of the model to predict crack growth under mode I/III and bending loading conditions. Unlike previous models[15], the proposed model incorporates a bending moment-rotation relation to transmit the moment and describe the initiation and propagation of cracks growing through the thickness of the shell elements. In addition, three-dimensional simulations of ductile crack propagation in elasto-plastic materials were used to emphasize the importance of plastic constrain in the region near the crack front. This numerical analysis revealed that the two-dimensional nature of shell elements together with the cohesive model is not appropriate to accurately predict the three-dimensional deformational state ahead of the crack front that evidently affects the overall behavior of the material. Therefore, the cohesive law for shells needs to be modified to take into account these geometry and material factors. For that reason, a scaling law for the cohesive strength is proposed in this work (see Figure 9). Future directions will be focused into a dimensional analysis where different geometry, as well as material parameters, will be included. Along these lines, it will be possible to come up with a dimensionless function for the "modified" cohesive strength as $\overline{T}_{\max}/\sigma_y = \Pi(t/l, E/\sigma_y, n, T_{\max}/\sigma_y)$, where the thickness t may be normalized by the ligament size (l) or the plastic zone length (Γ_p).

Finally, the versatility and ability of the model to predict crack growth under various loading conditions was then demonstrated in this work. This opens a new set of possible solutions for problems involving fracture in thin-walled structures that otherwise could not be solved with other models, such as dynamic impact and penetration of plates, deformation and failure of tubes and tearing of membranes. Figure 11 shows some preliminary simulations performed with this model for various materials.

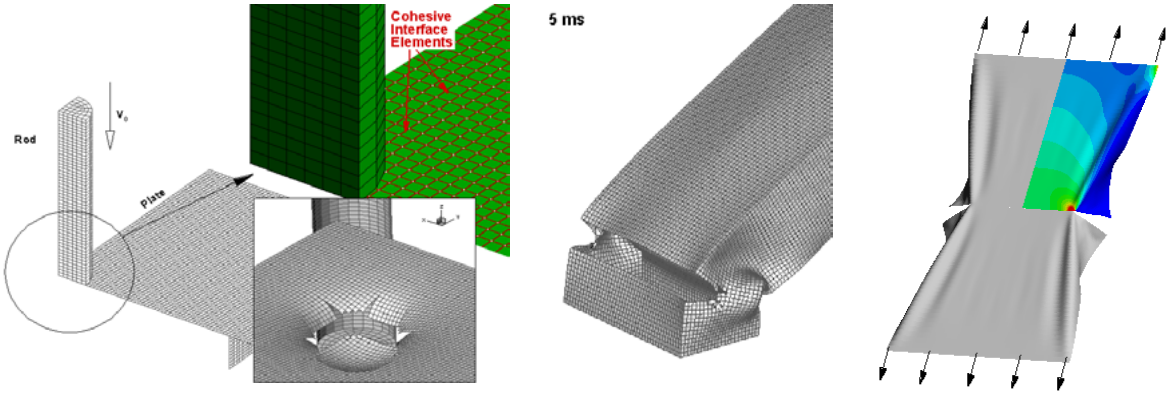

(a) (b) (c)

Figure 11: (a) Rod impacting a brittle plate. (b) Bending of an aluminum tube (c) Fracture of polymer membranes.

6 ACKNOWLEDGMENTS

The author would like to thank Prof. Marcos Actis and the *Departmento de Aeronautica* of *Universidad Nacional de La Plata, Argentina*, for their support during his stay, where the model was developed and implemented. He also would like to thank Nancy Johnson for helpful discussions and corrections of this paper.

7 REFERENCES

[1] G.I. Barenblatt, "The mathematical theory of equilibrium cracks in brittle fracture", Adv. Appl. Mech. 7, pp. 55-129, 1962.

[2] D.S. Dugdale, Journal of Mechanics of Physics of Solids, 8, pp. 100-104, 1959.

[3] Tvergaard V. and Hutchinson J.W., "The relation between crack growth resistance and fracture process parameters in elastic-plastic solids", J. Mech. Phys. Solids, 40, pp. 1377-1397, 1992.

[4] Xu X.-P and A. Needleman A. "Numerical simulations of fast crack growth in brittle solids", J. Mech. Phys. Solids, 42(9), pp. 1397-1434, 1994.

[5] Camacho G. and Ortiz M., "Computational modeling of impact damage in brittle materials", Int. J. Solids Structures, 33, pp. 2899-2938, 1996.

[6] H. D. Espinosa, P. D. Zavattieri and S. Dwivedi, "A finite deformation continuum/discrete model for the description of fragmentation and damage in brittle materials", J. Mech. Phys. Solids, 46(10), pp. 1909-1942, 1998.

[7] Zavattieri P.D. and Espinosa H.D., "Grain level analysis of ceramic microstructures subjected to normal impact loading", Acta Materialia, 49(20), pp. 4291-4311,2001.

[8] P.A. Klein, J.W. Foulk, E.P. Chen, S.A. Wimmer, H. Gao, "Physics-based modeling of brittle fracture: Cohesive formulations and the application of meshfree methods", Theoretical and Applied Fracture Mechanics, 37(1-3), pp. 99-166, 2001

[9] N. Moes, T. Belytschko, "Extended finite element method for cohesive crack growth", Engineering Fracture Mechanics, 69, pp. 813-833, 2002.

[10] De Borst, R. "Numerical aspects of cohesive-zone models", Eng. Fract. Mech., 70(14), pp.1743-1757, 2003 .

[11] M. Ortiz, A. Pandolfi, "Finite-deformation irreversible cohesive elements for three-dimensional crack-propagation analysis", Int. J. Num. Meth. Engrg. 44, pp. 1267-1282, 1999.

[12] A. Pandolfi, P.R. Guduru, M. Ortiz, A.J. Rosakis, "Three dimensional cohesive-element analysis and experiments of dynamic fracture in C300 steel",Int. J. Solids and Structures, 37, pp. 3733-3760, 2000.

[13] Zhou F. and Molinari J.F. "Dynamic crack propagation with cohesive elements: a methodology to address mesh dependency", Int. J. Numer. Meth. Engng, , 59, pp. 1-24 (2004).

[14] T. Belytschko, W.K. Liu, BG. Moran, "Nonlinear Finite Elements for Continua and

Structures", John Wiley & Sons, LTD, 2000.
[15] W. Li, T. Siegmund, "An analysis of crack growth in thin-sheet metal via a cohesive zone model", Eng. Fract. Mech., 69(18), pp. 2073-2093, 2002.
[16] Belytschko, Tsay, "Explicit algorithms for nonlinear dynamics of shells**",** Computational Methods in Applied Mechanics and Engineering**,** 43, pp. 251-276, 1984.
[17] Jerry Lin, "DYNA3D: A nonlinear, explicit, three-dimensional finite element code for solid and structural mechanics. User Manual", MDGME, LLNL. 1998.
[18] R.D. Mindlin, "Influence of rotary inertia and shear on flexural motions of isotropic, elastic plates", J. Appl. Mech. 18, pp. 31-38, 1951.
[19] J.R. Rice and N. Levy, "The part-through surface crack in an elastic plate", J. App. Mech, 39, pp. 185-194, 1972.
[20] D.M. Parks and C.S. White, "Elastic-plastic line-spring finite-elements for surface-cracked plates and shells", J. Press. Vessels, 104, pp. 287-292 1982.
[21] E. Mahgoub, X. Deng and M.A. Sutton, "Three-dimensional stress and deformation fields around flat and slant cracks under remote Mode I loading conditions" Eng. Fract. Mech, 70(18), pp. 2527-2542, 2003.
[22] S.W. Kwon, C.T. Sun, "Characteristics of three-dimensional stress fields in plates with a though-the-thickness crack", Int. J. Fract., 104, pp. 291-315, 2000.
[23] A.S. Gullerud, R.H. Doods Jr., R.W. Hampton, D.S. Dawicke, "Three-dimensional modeling of cutile crack growth in thin sheet metals: computational aspects and validation", Eng. Fract. Mech, 63, pp. 347-374, 1999.
[24] S. Roychowdhury, Y.D.Arun Roy, R.H. Doods Jr. "Ductile tearing in thin aluminum panels: experiments and analices using large-displacement, 3-D surface cohesive elements", Eng. Fract. Mech., 69, pp. 983-1002, 2002.
[25] K.K. Mathur, A. Needleman, V. Tvergaard, "Three dimensional analysis of dynamic ductile crack growth in a thin plate", J. Mech. Phys. Solids, 44(3),pp. 439-464, 1996.